ELSEVIER

Contents lists available at ScienceDirect

Ceramics International

journal homepage: www.elsevier.com/locate/ceramint



Effect of doping on the performance of high-crystalline SrMnO₃ perovskite nanofibers as a supercapacitor electrode



Gibin George^a, Shanell L. Jackson^a, Charles Q. Luo^a, Dong Fang^b, Duan Luo^c, Dongli Hu^c, Jianguo Wen^c, Zhiping Luo^a,*

- ^a Department of Chemistry and Physics, Fayetteville State University, Fayetteville, NC 28301, USA
- ^b College of Materials Science and Engineering, Kunming University of Science and Technology, Kunming 650093, PR China
- ^c Center for Nanoscale Materials, Argonne National Laboratory, Argonne, IL 60439, USA

ARTICLE INFO

Keywords: SrMnO₃ Doping Perovskite Electrospun nanofiber Supercapacitor Electrode

ABSTRACT

Perovskite oxides are promising multi-functional materials with enhanced physical and chemical properties. In this study, high-crystalline SrMnO $_3$ perovskite oxide nanofibers have been successfully synthesized by sol–gel electrospinning followed by calcination at different temperatures, using polyvinylpyrrolidone as a sacrificial polymeric binder. The change in porosity and grain size with calcination temperature imparted a substantial effect on the electrochemical properties of the obtained SrMnO $_3$ nanofibers. The SrMnO $_3$ nanofiber electrode calcined at 700 °C exhibits an electrochemical capacitance of 321.7 F g $^{-1}$ at a discharge current density of 0.5 A g $^{-1}$. The effect of doping Ba/Ca on Sr, and Co/Fe/Ni on Mn, respectively, on the specific capacitance of SrMnO $_3$ nanofibers is studied. 20 mol% Ba loading shows the best performance as a supercapacitor electrode with a specific capacitance of 446.8 F g $^{-1}$ at a discharge current density of 0.5 A g $^{-1}$. The nanofibers retained 87% its initial capacitance after 5000 successive cycles. The device fabricated using the nanofibers show an energy density of 37.3 W h kg $^{-1}$ at a power density of 400 W kg $^{-1}$, and it is retained as 15.7 W h kg $^{-1}$ even at a high-power density of 8006 W kg $^{-1}$, indicating the potential of this electrode material for high-rate charge/discharge operations in supercapacitors.

1. Introduction

The abrupt increases in energy demand and device miniaturization have given rise to a sudden urge to explore alternate sources of energy storage systems with high power density, high cyclic stability and fast storage while keeping at low costs. Supercapacitors are anticipated as promising energy storage devices with fast charging and power density adequate for small electronic devices, and they can fill the gap between the conventional capacitors and batteries [1]. The supercapacitance of an electrode material is associated with reversible faradic reactions of active species on the surface of the electrode [2]. The improvement of this synergic interaction between the electrode and electrolyte can ultimately enhance the supercapacitance. Nanosized materials with large surface areas and conductivities are primarily used as supercapacitor electrodes. The performance of transition metal oxides [3–5], various forms of carbon materials [6-8], conducting polymers [9] and their composites [10,11] have been investigated as supercapacitor electrodes. In spite of their poor conductivity, metal oxides exhibit large specific pseudocapacitance due to multi-electron transfer during the faradaic reactions [12], and also high power density and better stability than the organic electrochemical double-layer capacitor electrodes.

The supercapacitance of an electrode material is contingent to the number active sites on the electrode and ease of access to them by the electrolytic ions. The number of active sites are further determined by the integrity of the lattice and the numbers of oxygen vacancies and it increases remarkably with the decreasing dimensions of metal oxide crystals [13]. As the oxide supercapacitor materials store energy on their surfaces, the active materials as the electrodes with larger surface areas and porosity favor higher capacities during charge-discharge process. In order to increase the surface area and porosity, nanosized materials are often used as supercapacitor electrodes. The nanosized oxides of transition metals, such as MnO2 [3] NiO [4] and Co3O4 [5] have been extensively studied as supercapacitor electrode materials. Despite the nanosize, there are other ways to improve the electrodeelectrolyte interaction. The number of active sites on electrodes for the electrolyte ions can be improved either by defect engineering (doping, cationic vacancies, etc.), creating layered structures, or improving porosity.

E-mail address: zluo@uncfsu.edu (Z. Luo).

^{*} Corresponding author.

Recently, nanosized perovskite oxides with ABO₃ formula have been widely investigated for their applications in catalysis [14], water splitting [15], supercapacitance [16], batteries [17], optical [18], superconductivity [19], etc., and are considered to be a replacement for single oxides in the stipulated application. ABO₃ perovskites are promising for supercapacitance owing to the presence of multiple transition-metal ions in their crystal structure and therefore, perovskite oxides have the potential to enhance the performance of the supercapacitor through different charge storing mechanisms [20,21], by controlling the ratio of metallic ions used during the synthesis [22]. Moreover, perovskite oxides are capable of accommodating a large number of inherent oxygen vacancies [23].

The potential use of mixed-valent perovskite with trivalent lanthanide ion in the A site is extensively studied as supercapacitor electrode, e.g., LaFeO₃ [20], LaMnO₃ [21], LaCoO₃ [24], LaNiO₃ [25], etc. The LaMnO₃ possesses an orthorhombic structure, with space group of *Pbnm* and lattice parameters of $a = 5.531 \,\text{Å}$, $b = 5.602 \,\text{Å}$, and $c = 7.742 \,\text{Å}$ [26]. Doping these perovskites, where the divalent Sr ion incorporated in lanthanide perovskite lattice sites, for instance, $La_xSr_{1-x}NiO_{3-\delta}$ [27], $La_xSr_{1-x}CoO_{3-\delta}$ [28], $La_{0.85}Sr_{0.15}MnO_3$ [29], etc. enhanced the supercapacitor performance. On the other hand, the prospective of perovskites with SrBO₃ (B = Ti, Mn, Co, Fe, Ru, etc.) formulae with divalent Sr ions in the A site as supercapacitor electrodes is explored for $SrRuO_3$ [30], $SrTiO_3$ [31] and $SrCoO_{3-\delta}$ [16], and $SrFeO_3$ [32] and SrMnO₃ [33] are identified as the promising candidates. The SrMnO₃ possesses a hexagonal structure, with space group of P63/mmc and lattice parameters of $a = 5.443 \,\text{Å}$ and $c = 9.070 \,\text{Å}$ (refer to Results section of this paper). Besides supercapacitance, perovskites with SrBO₃ (B = Mn, Co, Fe, etc.) formulae have been reported as potential candidate for water splitting [34], solid state fuel cells [35], oxygen permeation [36], and gas sensing [37], etc.

In the present work, porous SrMnO₃, nanofibers were fabricated through a simple sol-gel assisted electrospinning process followed with calcination in air. SrMnO₃ consists of a three-dimensional network of MnO₆ octahedra and a large number of characteristic oxygen vacancies, leading to properties, such as, antiferromagnetism [38], electronic conductivity [39], thermochromism [40], etc. Doping with other elements ameliorate above said properties tremendously [41–43], because, the physico-chemical and transport properties are altered by the engineering of oxygen vacancies generated during doping. The generated oxygen vacancies show greater oxygen diffusion rates due to decreased transport lengths and it can ultimately improve the specific capacitance of metal oxide materials [44].

The morphology and texture of the SrMnO₃ nanofibers were controlled by calcining the electrospun precursor nanofibers at different temperatures to optimize the supercapacitance of the electrodes using cyclic voltammetric and charge-discharge measurements. The nanofibers with better specific capacitance are doped with Ba/Ca on Sr, and Co/Fe/Ni on Mn, respectively, through electrospinning process to compare the effect of dopants on the specific capacitance, since the oxygen vacancies of the material can be controlled by substitute ions at A or B sites of the perovskite materials [45,46]. Finally, the doped nanofibers with highest specific capacitance were further studied with different dopant loading. Although orthorhombic perovskite La₁- $_x$ Sr $_x$ MnO $_3$ (x = 0, 0.15, 0.3, 0.5) has been evaluated for supercapacitor [47], a study on high-crystalline hexagonal SrMnO₃-based perovskite nanofibers as a supercapacitor electrode material has not been reported in the literature. A supercapacitor based on the porous Ba doped SrMnO₃ nanofibers has been fabricated, and the performance is evaluated as a potential supercapacitor application. This work provides a facile strategy to synthesize other porous perovskite nanostructures.

2. Materials and methods

Polyvinylpyrrolidone (PVP) with mean molecular weight $\overline{M}_{\rm w}=1.3\times10^6,$ strontium (II) acetate (Sr(Ac)₂, assay 98%),

manganese (II) acetate ($Mn(Ac)_2$, assay 98%), N, N-dimethylformamide (DMF) and acetic acid purchased from Sigma Aldrich, were used without further purification to fabricate the precursor composite fibers. Na_2SO_4 procured from Acros Organics, and graphite sheets and activated carbon obtained from Alfa Aesar were used for the supercapacitance measurements.

To prepare electrospinnable sol of PVP and the metal salts, the respective acetate salts in the stoichiometric molar ratio of 1:1, in a total of 5 g, were dissolved first in a mixed solvent containing 50 mL acetic acid and 50 mL DMF. Further, 10 g PVP was added and stirred magnetically for 12 h before it was loaded to an electrospinning unit (MSK-NFES-4. MTI Corporation). The weight ratio of metal salts to PVP was 1:2. The electrospinning was carried out under an applied voltage of 18 kV, a tip to collector distance of 17 cm and a solution flow rate of 600 μL h⁻¹. The precursor composite fibers were randomly collected on a static collector plate. The electrospun PVP/Mn(Ac)2-Sr(Ac)2 composite nanofibers were then dried at 150 °C for 12 h. The fibers were subsequently calcined in air at 600, 700, 750 and 800 °C, respectively, and the obtained nanofibers are represented as SrMnO₃ @ 600, SrMnO₃@700, SrMnO₃@750 and SrMnO₃@800, respectively. The selection of the calcination temperature was based on the degradation temperature of the precursor composite fibers during their thermogravimetric analysis (TGA) (Shimadzu DTG-60) in a nitrogen atmosphere at a heating rate of 10 °C min⁻¹. The calcination was carried out at a heating rate of 1 °C min⁻¹ with dwell time of 6 h at the calcination temperature to obtain SrMnO3 perovskite nanofibers. The doped nanofibers were made using the similar method, in which respective molar percentage of acetate salts of the dopants are added to replace the subsequent amount of Sr(Ac)2, and the aforesaid procedure was followed. All the doped SrMnO₃ and BaMnO₃ nanofibers were calcined at 700 °C.

The morphology of the nanofibers obtained at different calcination temperatures were examined by a field-emission JEOL JXA-8530F electron probe microanalyzer (EPMA) for imaging in the scanning electron microscope (SEM) mode, equipped with an X-ray energy-dispersive spectrometer (EDS) for chemical compositional analysis. The samples were coated with ~ 10 nm carbon prior the EPMA analysis. The nanofibers for transmission electron microscopy (TEM) were prepared in pure ethanol solutions, sonicated for 1 min and then dispersed on carbon-film supported grids. The grids were observed in the Argonne chromatic aberration-corrected TEM (ACAT, a FEI Titan 80-300 ST) with both spherical C_s and chromatic C_c aberration corrections at 200 kV. The X-ray diffraction (XRD) patterns of the nanofibers were recorded using Rigaku MiniFlex 600 X-ray diffractometer in a scan range of 10–90° and a scan speed 0.06° min⁻¹. To determine the change in lattice parameter and the unit cell volume after doping, the XRD patterns are refined by Rietveld method using PDXL2 software by Rigaku. Fourier-transform infrared (FTIR) spectra (IRPrestige-21, Shimadzu) were recorded in transmission mode by KBr pellet method in the wave number range of 300–4000 cm⁻¹ at an average of 32 scans.

The electrodes for supercapacitance measurements were prepared on graphite sheet (GS) cut to the size 1 cm \times 1 cm. To modify the GS as working electrodes, a slurry in DMF containing the nanofiber, activated carbon and polyvinylidene fluoride in the ratio 80:15:5 were prepared in a mortar and pestle and applied to the GS and then dried in air, 1 mg of active material was loaded to the GS working electrodes. These electrodes were soaked in 0.5 M Na₂SO₄ for 30 min to attain equilibrium before supercapacitance measurements. The electrochemical studies were performed using a three-electrode system with modified GS electrode with an effective surface area of 1 cm² as the working electrode, platinum wire as the counter electrode and Ag/AgCl as the reference electrode. The supercapacitive studies of modified GS electrodes with nanofibers calcined at different temperatures were performed under 0.5 M Na₂SO₄ medium, using a computer-controlled potentiostat/galvanostat (CH Instruments, USA). An asymmetric supercapacitor was fabricated using the nanofiber modified GS as positive electrode and activated carbon loaded GS as negative electrode. These electrodes were separated by Whatman filter paper soaked in $0.5\,\mathrm{M}$ $\mathrm{Na_2SO_4}$ medium.

3. Results and discussion

The TGA and DTA plots of PVP/Sr(NO₃)/Mn(NO₃)₂ composite nanofibers are shown in Fig. S1. The composite nanofibers exhibit three-step degradation before it is completely transformed to SrMnO₃ nanofibers, whereas the pure PVP exhibit a single step in its thermal degradation profile [48]. The actual onset of degradation of the nanofibers is at 300 °C and the degradation is completed at 500 °C. The First step in the degradation process at ~ 100 °C is due to the removal of water from the nanofibers. The second step in the degradation process can be linked to the conversion of the acetate salts to the respective carbonates and the complete degradation of the organic phases takes place in the final step. The DTA curve reveals the occurrence of multiple exothermic and endothermic phase transformations during the degradation process. Though there is no remarkable weight loss above 500 °C, the phase transformation is perceptible from the DTA peaks above 500 °C.

3.1. Morphology and structure

The successful transformation of the precursor composite fibers to SrMnO₃ perovskite nanofibers was confirmed with the XRD analysis as shown in Fig. 1a. The very sharp peaks in the XRD patterns of the calcined nanofibers reveal the crystalline nature of the obtained nanofibers. The obtained SrMnO₃ structure can be indexed to JCPDS standard data file No. 01-084-1612, with space group of $P6_3/mmc$ ($a=5.443\,\text{Å}$ and $c=9.070\,\text{Å}$). On comparing the XRD patterns of the obtained SrMnO₃ nanofibers calcined at different temperatures, it is observed that the pure SrMnO₃ phase is formed at 700 and 750 °C. The XRD pattern of the nanofibers calcined at 800 °C reveals the transformation of hexagonal SrMnO₃ to Sr₇Mn₄O₁₅ or Sr₄Mn₃O₁₀ phase. At a calcination temperature of 600 °C, the degradation of polymeric part is completed, but the presence of strontium carbonate is identified in the respective pattern.

XRD patterns of the doped SrMnO₃ nanofibers are shown in Fig. 1b. Upon doping with various elements (Ba, Ca, Co, Fe, and Ni) in SrMnO₃ nanofibers the crystal structure of SrMnO₃ remains unaffected until 20 mol% loading of the dopants, Fig. 1b, as there is no apparent peak of the dopant oxide in the XRD pattern of the respective nanofibers. Representative Rietveld refined XRD patterns of doped SrMnO₃ nanofibers are shown in Fig. 2, and the estimated lattice parameter and unit cell volume are presented in Table 1. The refined weighted-profile factor

 $R_{\rm wp}$ and profile factor $R_{\rm p}$ are indicated in Fig. 2 and Table 1. One can observe a remarkable difference in the lattice parameters of the doped SrMnO₃ nanofibers as compared with pure SrMnO₃ nanofibers. This change in the lattice parameters is attributed to the difference in the atomic radii of the dopant ions with respect to the parent ions. While the Ba loading is increased to 50 mol%, additional peaks are originated, which can be attributed to the formation of BaMnO₃ structure as in Fig. S2. On further increase of Ba loading to 75 mol%, a significant change in the XRD pattern is observed as compared with pure SrMnO₃ structure. The new phase appeared in the pattern of 75 mol% Ba doped SrMnO₃ is Ba₃Mn₂O₈ (JCPDS data file No.). Nanofibers with pure Ba₃Mn₂O₈ and BaMnO₃ structure are also successfully produced. The XRD patterns of Ba₃Mn₂O₈ and BaMnO₃ nanofibers can be indexed to PDF cards 2008132 and 026-0168, respectively.

The representative TEM images of the calcined $SrMnO_3@700$ nanofibers are shown in Fig. 3. The TEM images reveal that the nanofibers are polycrystalline in nature, with a grain size ~ 30 nm (Fig. 3a). The electron diffraction pattern in Fig. 3b shows a ring pattern from polycrystalline nanocrystals with high crystallinity, which is indexed as the hexagonal structure being consistent with the XRD. Grains are randomly oriented in the nanofiber and they are formed during the pyrolysis of the composite nanofibers, due to homogeneous nucleation and the space confinement of the nanofibers [49]. The measured d-spacings from the high-resolution TEM (HRTEM) image (Fig. 3c) are consistent with the XRD results.

Fig. 4a-c shows the SEM images of randomly oriented nanostructured SrMnO3 nanofibers obtained at different calcination temperatures. One can observe a significant difference in the morphology/ texture of the nanofibers obtained after calcination at each temperature. On comparing the surface texture (Figs. 4, 5) of the nanofibers obtained at different calcination temperatures, the surface SrMnO₃@ 600 nanofibers is smooth and there is no clear evidence of highly porous structure within the nanofibers. While in the sample of SrMnO₃@700nanofibers, one can distinguish the highly porous nature of the nanofibers, composed of myriads of small grains. However, SrMnO₃@800 nanofibers are composed of large grains with a smaller nanofiber diameter. The SEM images of the representative doped SrMnO₃ nanofibers calcined at 700 °C are shown in Fig. S3a and b. The doped nanofibers also retained the continuous-long fibrous morphology, however, the BaMnO₃ nanofibers shown in Fig. S3c has a beaded morphology. In the EDS spectrum (Fig. S4) of the representative nanofibers, the peaks corresponding to Sr, Mn and O and the representative dopants are present. The representative elemental maps of the pure and doped nanofibers are shown in Figs. S5-S6.

The complete elimination of organic parts from the precursor composite fibers is confirmed with the FTIR spectra (Fig. S7). In all the

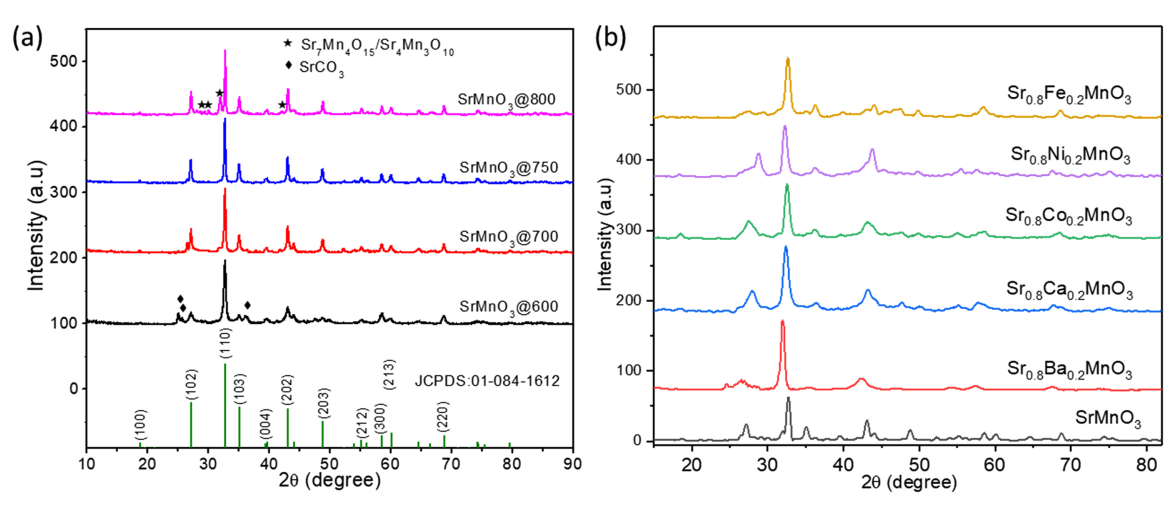


Fig. 1. Comparison of XRD patterns of (a) SrMnO₃ nanofibers calcined at different temperatures, and (b) doped SrMnO₃ nanofibers calcined at 700 °C.

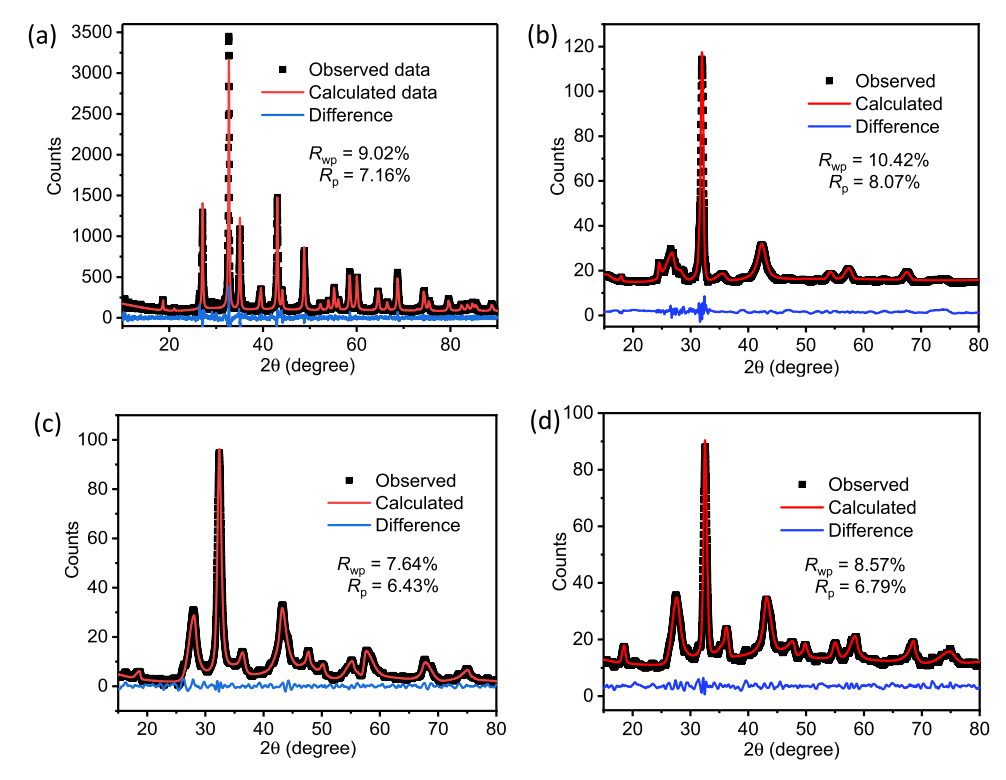


Fig. 2. Rietveld refined XRD patterns of pure and representative doped $SrMnO_3$ nanofibers. (a) $SrMnO_3@700$, (b) $Sr_{0.8}Ba_{0.2}MnO_3$, (c) $Sr_{0.8}Ca_{0.2}MnO_3$, and (d) $SrMn_{0.8}Co_{0.2}O_3$ nanofibers.

Table 1 Lattice parameter and unit cell volume of pure and doped $SrMnO_3$ nanofibers estimated after Rietveld refinement.

Nanofiber	a (Å)	b (Å)	c (Å)	R _{wp} (%)	R _p (%)	Volume of unit cell (cubic Å)
SrMnO ₃ @700	5.454	5.454	9.086	9.02	7.16	234.0566
Sr _{0.8} Ba _{0.2} MnO ₃	5.544	5.544	9.162	10.42	8.07	243.8679
Sr _{0.8} Ca _{0.2} MnO ₃	5.417	5.417	8.869	7.64	6.43	225.3772
SrMn _{0.8} Co _{0.2} O ₃	5.475	5.475	9.027	8.57	6.79	234.6015
SrMn _{0.8} Ni _{0.2} O ₃	5.498	5.498	8.979	10.17	7.86	235.0473

FTIR spectra, the peaks between $3600-3085\,\mathrm{cm}^{-1}$ are due to the adsorbed water molecules. In the IR spectrum of PVP/Sr(Ac)₂-Mn(Ac)₂ nanofibers, the peaks at 2957 and 2890 cm⁻¹ represent the symmetric and asymmetric vibrations of CH in CH₂ and CH₃, respectively. The peaks 1648, 1562, 1439 and 1287 cm⁻¹ are attributed to C=O, C=C stretching in aromatic rings, CH₂ bending and C=N vibrations, respectively [50]. The broad peak between 800 and 400 cm⁻¹ is due to the several vibrational modes of pyrrolidone ring [51]. On comparing

the IR spectrum of the PVP/Sr(Ac)₂-Mn(Ac)₂ composite nanofibers with those of SrMnO₃@600 and SrMnO₃@700, as in Fig. S7a, the characteristic IR peaks of PVP disappear. There is a strong evidence on the presence of SrCO3 in SrMnO3@600 nanofibers as detected in the XRD data. In the IR spectrum of SrMnO₃@600 nanofibers, the observed peaks at 1671, 1467 1188 cm⁻¹ and 984 cm⁻¹ are originated from C=O, C-OH and C-O stretching, respectively [50], corresponding to SrCO₃ and the remaining peaks, 642 and 532 cm⁻¹ are due to the Mn-O stretching in MnO₆ octahedra, Mn-O-Mn bending [52], respectively, from the SrMnO₃ structure. The IR spectrum of SrMnO₃@700 nanofibers exhibits peaks from SrMnO3 structure only. From Fig. S7b, the peaks originated by Mn-O-Mn bending and Mn-O stretching in SrMnO₃ are modified in the presence of dopants. The shift in Mn-O stretching peaks and modification of Mn-O-Mn bending peak can be associated with dopant induced defects in those fibers [53]. It is worthwhile to note that pure SrMnO₃@700 and BaMnO₃ nanofibers exhibit well-defined peaks corresponding to and Mn-O stretching and Mn-O-Mn bending vibrations.

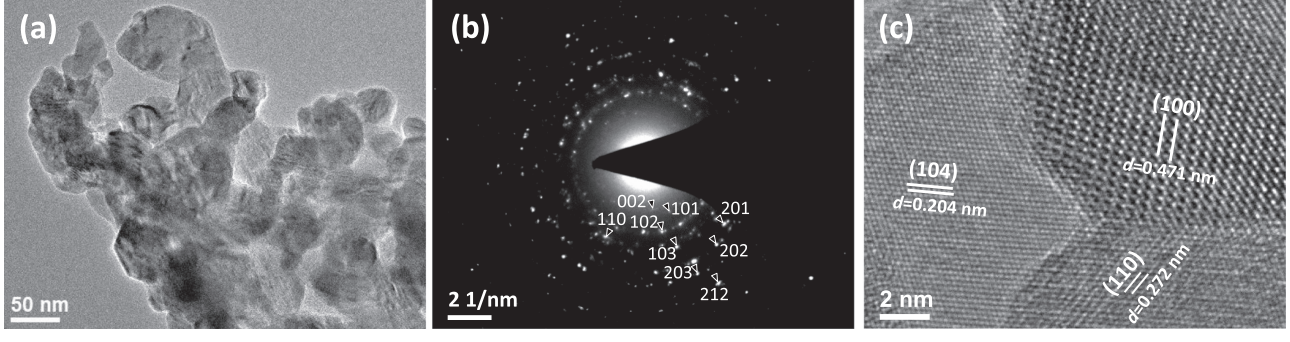


Fig. 3. (a) TEM, (b) SAED pattern, and (c) HRTEM images of SrMnO₃@700 nanofibers.

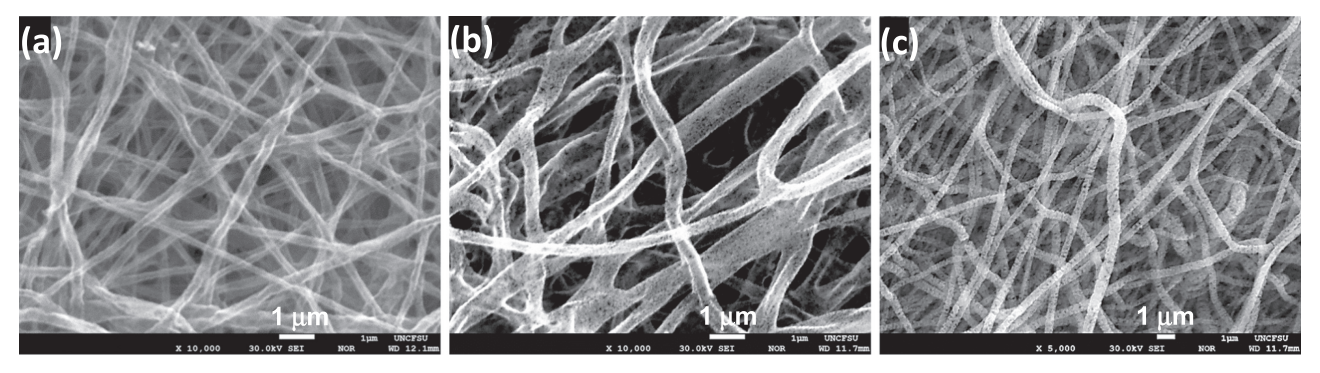


Fig. 4. SEM images of (a) SrMnO₃@600, (b) SrMnO₃@700, and (c) SrMnO₃@800 nanofibers.

3.2. Electrochemical characterization of SrMnO₃ perovskite nanofiber

The electrochemical properties of the SrMnO₃ nanofibers calcined at different temperatures and Ba, Ca, Co, Fe and Ni doped SrMnO3 nanofibers as a supercapacitor electrode is studied using cyclic voltammetry (CV), Galvanostatic charge-discharge curves (GCD) and electrochemical impedance spectroscopy (EIS) techniques. The area under the cyclic voltammogram is a measure of electrochemical charge storage capacity of the electrode [54]. The representative cyclic voltammograms of the as-fabricated SrMnO₃ nanofiber calcined at 600, 700 and 800 °C are compared in Fig. 6a, in 0.5 M Na₂SO₄ (aq.) recorded at a scan rate of $10\,\mathrm{mV}\,\mathrm{s}^{-1}$ for the same mass loading. In all the voltammograms, the voltammetric current is directly proportional to the scan rate. The voltammograms has the shapes close to the electric double layer capacitance, without any superficial Faradaic oxidation/reduction peaks. The symmetry of the cyclic voltammograms indicates the reversibility of the electrodes for charging and discharging cycles. The voltammetric curves of the electrospun SrMnO₃ electrode exhibit a nearly rectangular shape in the applied potential range, which is an indicative of an ideal capacitor with a compromise of both pseudocapacitive and double layer capacitance. The symmetry between cathodic and anodic regime is concomitant to the fast-reversible process of ionic intercalations on electrode surface. The transition of manganese oxidation states between Mn³⁺↔Mn⁴⁺ alleviates the ionic intercalation/deintercalation over electrode material. While comparing the area of cyclic voltammograms of nanofibers obtained at different calcination temperatures, the $\rm SrMnO_3@700$ electrode has the largest area at a scan rate of 10 mV s $^{-1}$, indicating the good capacitive capability of those nanowires. The better performance of $\rm SrMnO_3@700$ can be attributed to the high porosity of these nanofibers as observed in SEM images, and the pure $\rm SrMnO_3$ phase is observed in SrMnO_3@700 nanowires from the XRD analysis. $\rm SrMnO_3@700$ electrode could have the best electrochemically active surface with good accessibility to the ions, and one can expect enhanced capacitive behavior than the nanofibers obtained at other calcination temperatures.

The variation in the Galvanostatic charge-discharge (GCD) cycles of the electrodes calcined at different temperatures at a current density of $0.5\,\mathrm{A\,g^{-1}}$ is shown in Fig. 6b. The near linear range in the triangular GCD curves indicates the electrochemical double-layer capacitance behavior, which may take place at the interface between electrode and electrolyte [55].

The specific capacitance is calculated according to the following equation from the charge discharge curves [56]:

$$C_{\rm sp} = I\Delta t/mV \tag{1}$$

where, $C_{\rm sp}$ is the specific capacitance (F g⁻¹), I is the discharge current, Δt is the discharge time and m is the mass of the active materials (in g) and V is the potential window, respectively.

The specific capacitance values of the $SrMnO_3$ electrodes at different current densities are shown in Fig. 6c. The electrospun $SrMnO_3$ supercapacitor electrode exhibits a remarkable specific capacitance, which is dropped at high current densities by $\sim 60\%$. As expected from

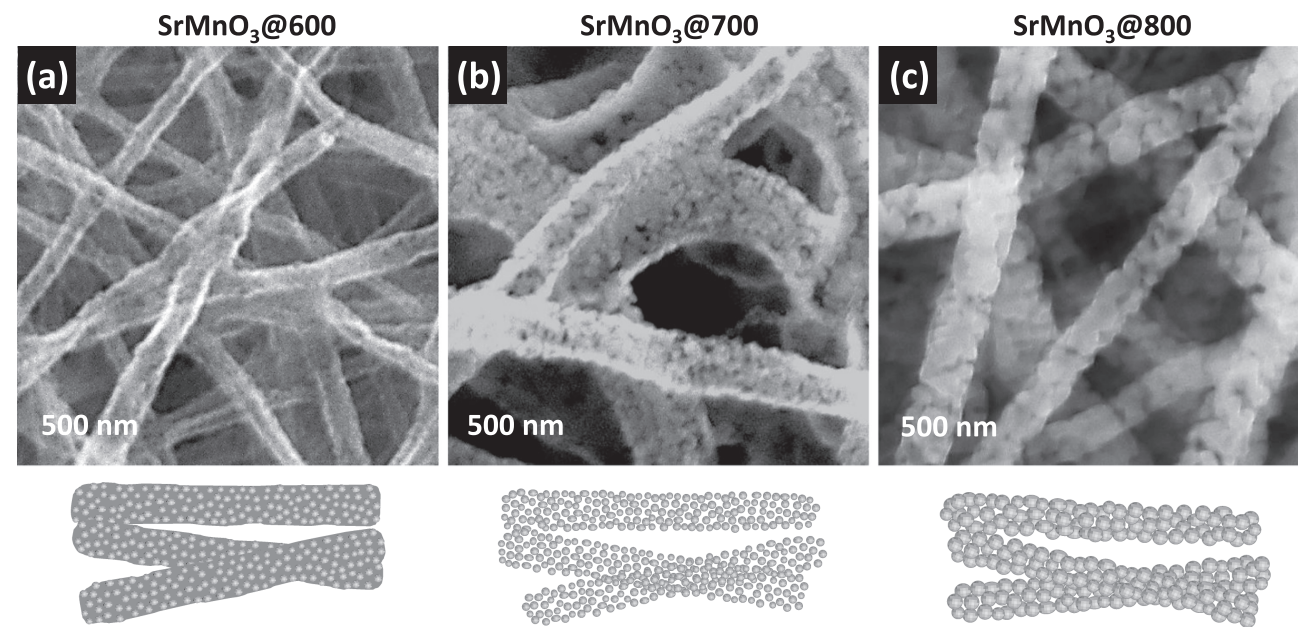


Fig. 5. Enlarged SEM images (top) and schematic illustrations of the texture of the SrMnO₃ nanofibers obtained at 600 °C (a), 700 °C (b) and 800 °C (c).

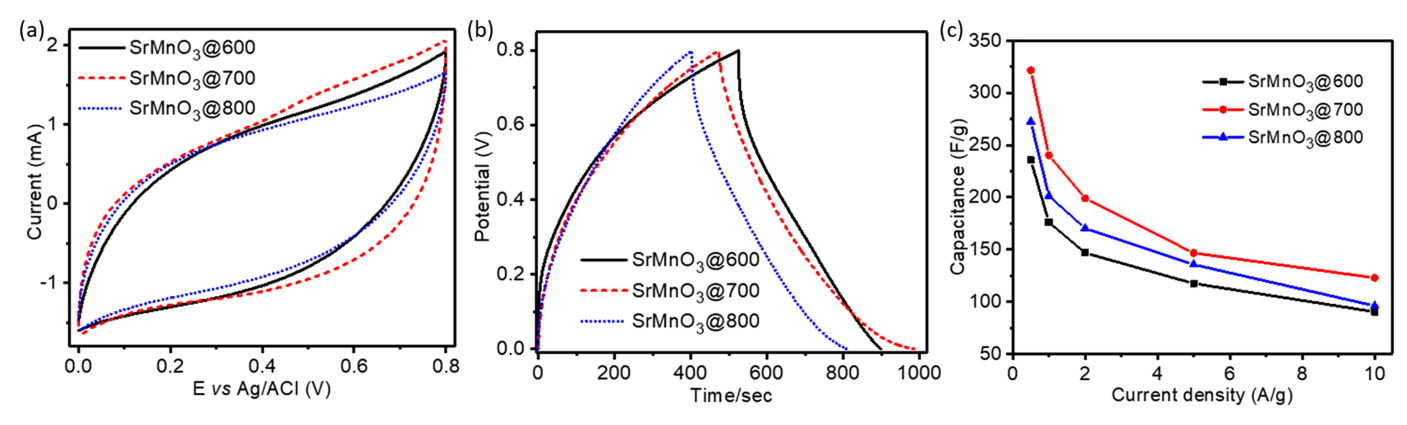


Fig. 6. (a) CV (scan rate = $10\,\mathrm{mV\,s^{-1}}$) (b) GCD curves (current density = $0.5\,\mathrm{A\,g^{-1}}$), and (c) specific capacitance of SrMnO₃ nanofibers calcined at different temperatures.

Table 2 The specific capacitance $(F\,g^{-1})$ of nanofiber electrodes at different current densities.

Nanofiber	Current Density (A g ⁻¹)						
	0.5	1	2	5	10		
SrMnO ₃ @600	235.6	176.2	146.8	117.5	90.4		
SrMnO ₃ @700	321.7	240.4	199.0	146.7	122.9		
SrMnO ₃ @800	272.7	201.4	170.3	135.7	96.2		
$Sr_{0.8}Ca_{0.2}MnO_3$	338.2	242.7	202.1	147.3	120.3		
$SrMn_{0.8}Co_{0.2}O_3$	418.4	312.4	258.4	189.9	158.5		
$SrMn_{0.8}Fe_{0.2}O_3$	345.6	257.5	213.3	156.4	119.1		
$SrMn_{0.8}Ni_{0.2}O_3$	354.6	229.9	218.5	166.2	127.0		
$Sr_{0.9}Ba_{0.1}MnO_3$	372.7	273.4	211.1	168.6	134.1		
$Sr_{0.8}Ba_{0.2}MnO_3$	446.8	333.2	270.8	196.7	161.0		
$Sr_{0.7}Ba_{0.3}MnO_3$	375.9	276.4	218.4	159.7	134.6		
$Sr_{0.5}Ba_{0.5}MnO_3$	261.4	190.2	154.3	115.5	93.6		
$Sr_{0.25}Ba_{0.75}MnO_3$	177.5	130.2	100.3	80.3	63.8		
$Ba_3Mn_2O_8$	241.0	177.2	140.6	102.4	86.3		
$BaMnO_3$	216.8	162.1	131.8	95.2	77.84		

CV data, SrMnO₃@700 has the highest capacitance (Table 2), which may be attributed to the better morphological and structural parameters such as surface area, pore size, and crystallite size. The high porosity and surface area are likely to improve the double layer capacitance through more ion diffusion and adsorption in the charge-discharge process. Moreover, with high porosity, sufficient electrochemically active sites are exposed that can hold a large quantity of electrolyte and thereby providing more electrode–electrolyte accessibility [57,58].

To explore the effect of doping on SrMnO₃ nanofibers, a calcination temperature of 700 °C is selected as the optimum calcination temperature. Ba, Ca, Co, Fe and Ni are selected as the doping elements for the present study. The elements Ba and Ca replaces Sr site (A site) and the elements Co, Fe and Ni replaces the Mn site (B site) in the SrMnO₃ perovskite lattice. The cyclic voltammograms of SrMnO3 nanofibers doped with 20 mol% of Ba, Ca, Co, Fe and Ni are compared in Fig. 7a, recorded at a scan rate of 10 mV s⁻¹. The shape of the CV curves is unaltered as compared with the pure SrMnO₃, though the area under the CV curve is increased after doping. On doping the elements, Ba, Ca, Co, Fe and Ni, in SrMnO₃, the specific capacitance is increased than pure SrMnO₃ nanofibers. On comparing the GCD curves (Fig. 7b) of the doped nanofibers, a longer charging and discharging time is observed than the pure SrMnO₃ nanofibers calcined at 700 °C and therefore a higher specific capacitance. The specific capacitance at different current densities are shown in Fig. 7c. The highest specific capacitance is observed on Ba doping among the above doped nanofibers, as presented in Table 2. The performance of perovskite materials as supercapacitor electrodes is owing to their inherent nature to comprise oxygen

vacancies as the charge carriers [47]. The amount of oxygen vacancies can be tailored by doping as the dopant ions with a different ionic radius than the parent ion can generate lattice distortions and an increased oxygen vacancies in oxides [59]. In the present study, the ionic radius of Ba is higher than the other dopants and therefore more oxygen vacancies are plausibly generated as charge carriers.

While increasing the Ba loading, the CV curves (Fig. 7d) are identical to that of $SrMnO_3$ without any significant oxidation or reduction peaks. The Galvanostatic charge discharge cycles (Fig. 7e) reveals the near symmetric charge-discharge pattern from all the fibers. The specific capacity (Fig. 7f) calculated from GCD curves tends to decrease at higher Ba loading, which can be attributed to more lattice distortions and thereby reduced oxygen adsorption in those fibers [47]. The specific capacity of pure BaMnO $_3$ and Ba $_3Mn_2O_8$ nanofibers are lower than the pure and 20 mol% Ba loaded $SrMnO_3$ nanofibers.

In SrMnO3 structure Mn (IV) is the Jahn-Teller-ion when it is replaced by other elements, and thus the oxygen framework of the perovskite structure is distorted [60]. The lattice distortion is possible by introducing other elements analogous to the incorporation of Ba or Ca in place of Sr. As the ionic radius of Ba (II) (1.35 Å) is bigger than that of Sr (II) (1.18 Å), lattice expansion in the perovskite structure is expected when doped with Ba, while lattice contraction when doped with Ca (1.0 Å), therefore, resulting a larger lattice parameter in Ba doped SrMnO₃ nanofibers than that of pure SrMnO₃ nanofibers as presented in Table 1. The lattice expansion may create more oxygen vacancies and consequently Mn (III) ions to balance the charge. The oxygen vacancy sites in turn have a strong affinity towards electrolyte anions. Hence the vacancy occupied by anionic intercalation followed by a change in oxidation states of Mn atom $(Mn^{3+} \rightarrow Mn^{4+})$, ultimately augments the pseudocapacitance of the Ba doped SrMnO3 nanofibers [61]. On the other hand, when SrMnO3 is doped with Co, Fe and Ni where Mn is replaced by these dopants, only octahedral distortions are expected and the change in lattice parameters is insignificant as evident in Table 1, so they showed lower pseudocapacitance than Ba doped SrMnO₃.

On comparing the Galvanostatic charge-discharge measurements of the as prepared nanofibers calcined at different temperatures and different compositions at a current density of $0.5\,\mathrm{A\,g^{-1}}$ as in Figs. 6b and 7b&e, one can observe the near symmetric nature of the curves and the highest capacitance was obtained for a current density of $0.5\,\mathrm{A\,g^{-1}}$. The near symmetric charge-discharge curves indicate the electrochemical reversibility of the electrode materials. The symmetry of the charge-discharge curves is different for the nanofibers with different composition. The change in symmetry of the charge-discharge curves can be coupled with the interaction of electrodes with the cations of the electrolyte. The accessibility of the cations to the active surfaces are influenced by the impurity present in the fibers. The change in the symmetry of the charge-discharge curves are accurately estimated in terms of the coulombic efficiency [62]. The coulombic efficiency was

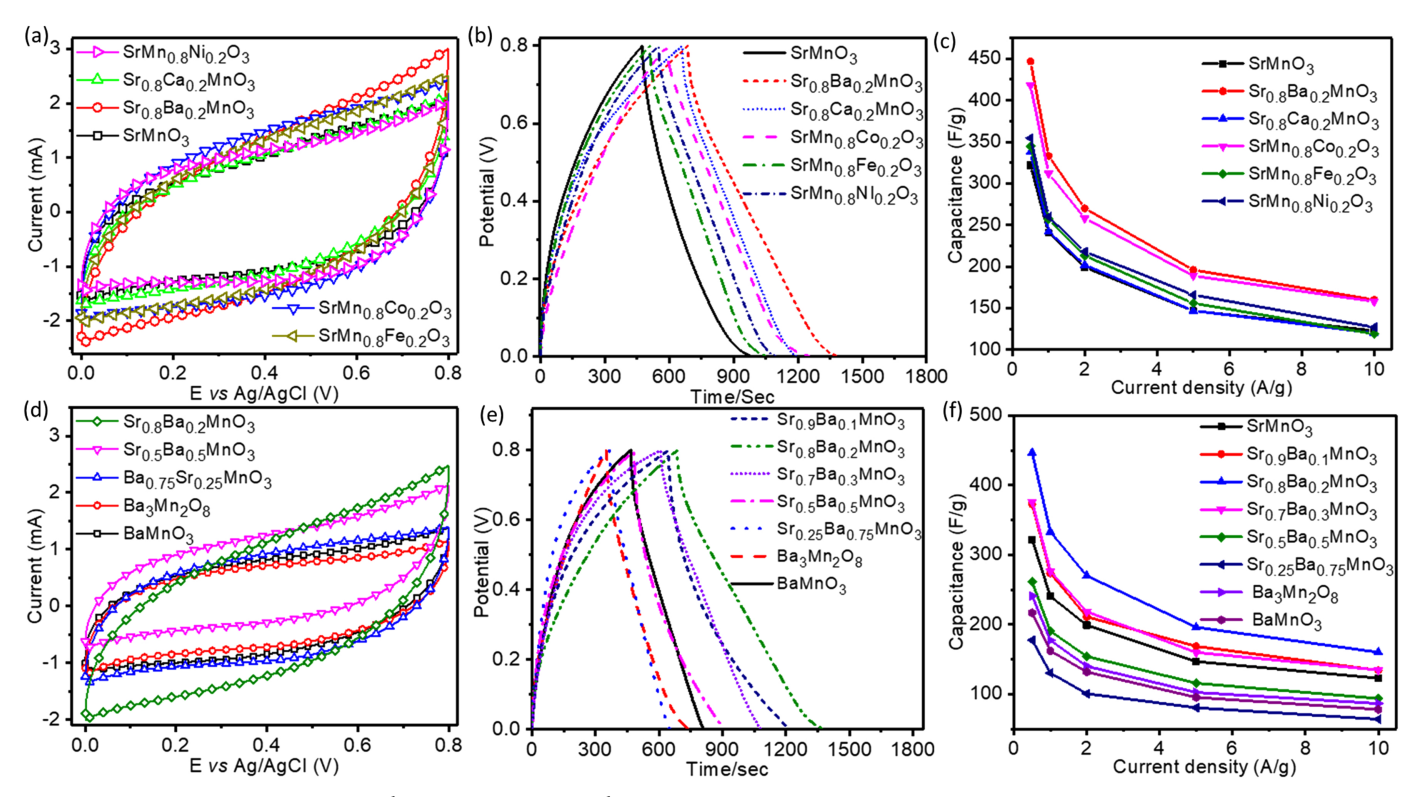


Fig. 7. Comparison of (a, d) CV (10 mV s^{-1}) , (b, e) GCD (0.5 A g^{-1}) , and (c, f) specific capacitance of doped-SrMnO₃ and Ba-doped supercapacitor electrodes, respectively.

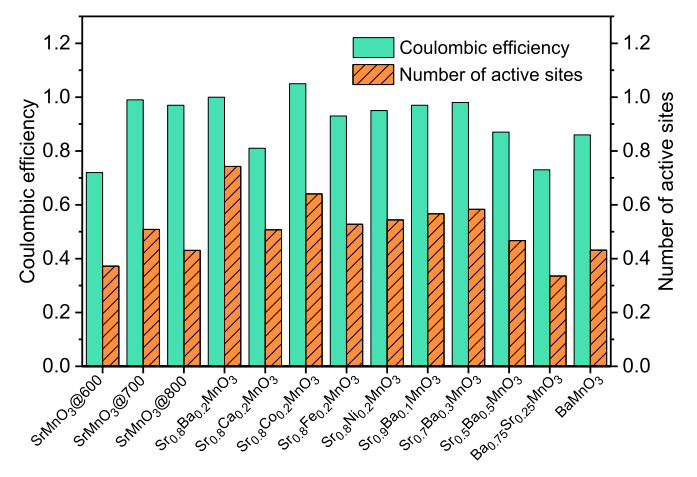


Fig. 8. Coulombic efficiency and available active sites for the nanofibers.

compared among the nanofibers fabricated in this study for a charge and discharge current density of $0.5 \,\mathrm{A\,g^{-1}}$ using the relation (Fig. 8),

$$\eta = \frac{t_{\rm d}}{t_{\rm c}} \times 100 \tag{2}$$

where, η is the columbic efficiency, $t_{\rm d}$ is the discharging time, and $t_{\rm c}$ is the charging time.

The conductivity and ease of mobility of the cations within the electrode surface determines the performance of the electrode. The electrode performance can be evaluated by calculating the active sites on the electrodes (Fig. 8). The highest number of active sites are obtained for nanofibers with highest specific capacitance, which can be corroborated to the morphological/compositional properties of those nanofibers. The available active sites (Z) are determined from the specific capacitance of the nanofiber electrodes using the following equation [63]:

$$Z = \frac{C_{\rm sp} \Delta VW}{F} \tag{3}$$

where, $C_{\rm sp}$ is the specific capacitance, ΔV is the potential window, W is the molecular weight of nanofiber material, and F is the Faradaic constant

The impedance behavior of the nanofiber/GS electrodes was measured in the frequency range of 1-100 kHz with an amplitude of 5 mV and the corresponding Nyquist plots are shown in Fig. 9. The impedance spectra of the all as synthesized nanofibers exhibit a straight line at the low-frequency and a quasi-semicircle at high-frequency regime. The impedance data are fit to an equivalent Randles circuit as shown in Fig. 9d. The Randles circuit has the following components. The charge transfer resistance (R_{ct}) corresponding to the diameter of the semicircle at high frequency region at the electrode-electrolyte boundary, i.e., resistance to the diffusion of ions at the interface between the electrode and electrolyte [64]. The changes in R_{ct} in the reported samples are due to the different level of distortion of the electron conduction path (Mn-O-Mn bonds), caused by dopants [65]. As insignificant semi-circles at high frequencies were observed, it indicated a negligible charge-transfer resistance across the interface of nanofibers/electrolyte [66]. The lowest $R_{\rm ct}$ values are observed for Sr_{0.8}Ba_{0.2}MnO₃ electrodes shows a smaller charge transfer resistance than the nanofibers with other compositions. The slope of the impedance in the low frequency region correspond to the mass transfer rate of the electrolyte in the pores and diffusive resistance of the electrolyte in the electrode pores, Warburg impedance (Z_w) . The solution resistance (R_s) is obtained from the intersection of the high frequency side with the horizontal axis of the Nyquist plot [67]. Therefore, the electrode with small charger transfer resistance and low diffusive resistance may increase the synergic interaction with the electrolyte. Table 3 shows the parameters obtained by fitting the equivalent circuit model. $C_{\rm p}$ is the pseudocapacitance component, and $C_{\rm dl}$ is double layer capacitance. In La_{1-x}Sr_xMnO₃ perovskite system, the partial substitution of Sr increases the conductivity of the system with a maximum

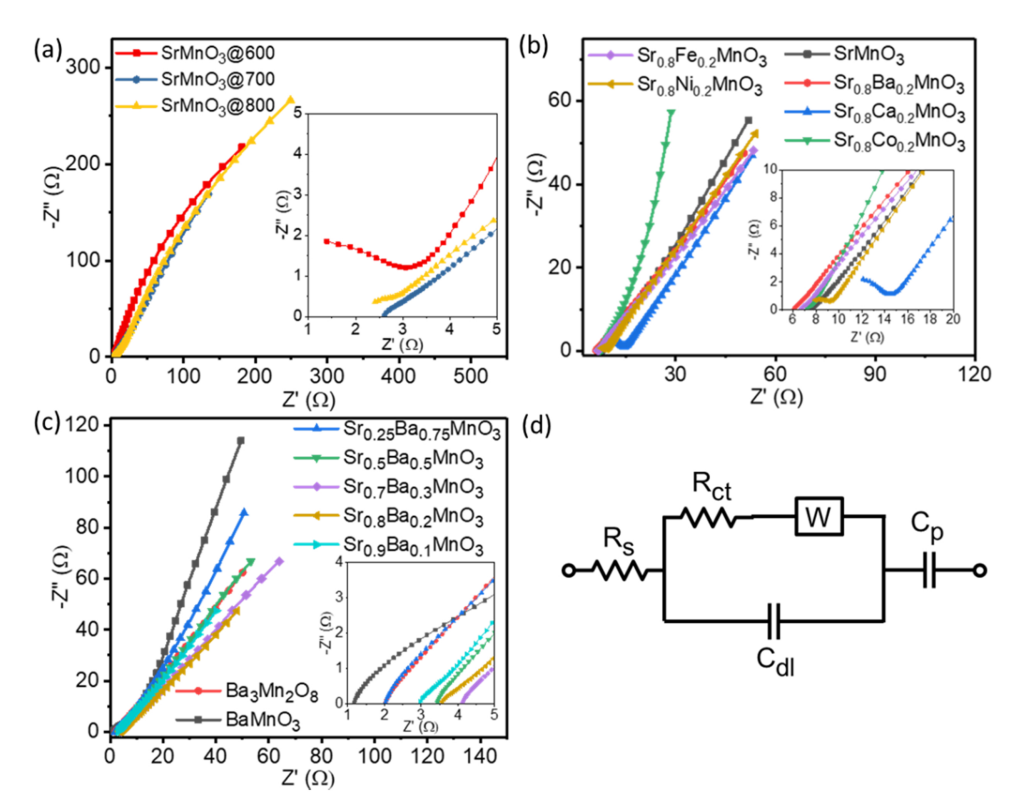


Fig. 9. EIS spectra of (a) SrMnO₃ nanofibers calcined at different temperatures, (b) SrMnO₃ doped with different elements, (c) pure BaMnO₃ and Sr doped BaMnO₃, and (d) equivalent Randles circuit.

 Table 3

 Values of equivalent circuit components of EIS spectra.

Nanofiber	$R_{\mathrm{ct}}\left(\Omega\right)$	$C_{ m dl}$ (μF)	$R_{\rm s}\left(\Omega\right)$	$Z_{ m w}$	$C_{\rm p}$ (mF)
SrMnO ₃ @600	2.21	25.4	13.2	0.001	15.4
SrMnO ₃ @700	0.65	32.7	7.6	0.008	23.2
SrMnO ₃ @800	0.84	28.8	8.6	0.005	11.6
$Sr_{0.8}Ca_{0.2}MnO_3$	2.03	22.2	8.3	0.005	18.9
$SrMn_{0.8}Co_{0.2}O_3$	0.54	30.5	8.1	0.002	53.5
$SrMn_{0.8}Fe_{0.2}O_3$	1.2	24.6	6.7	0.006	35.8
$SrMn_{0.8}Ni_{0.2}O_3$	2.02	23.8	6.4	0.007	41.9
$Sr_{0.9}Ba_{0.1}MnO_3$	0.73	20.8	5.1	0.007	39.4
$Sr_{0.8}Ba_{0.2}MnO_3$	0.33	24.73	4.1	0.006	74.4
$Sr_{0.7}Ba_{0.3}MnO_3$	0.63	29.73	6.3	0.006	56.7
$Sr_{0.5}Ba_{0.5}MnO_3$	0.56	26.5	7.6	0.006	16.6
$Sr_{0.25}Ba_{0.75}MnO_3$	1.15	29.5	8.1	0.005	14.2
$Ba_3Mn_2O_8$	1.89	22.1	6.7	0.005	13.8
$BaMnO_3$	1.93	28.3	5.3	0.010	16.3

conductivity correspond to x=0.15 [47] and those samples exhibit the highest specific capacitance than pure LaMnO₃. The capacitance of La_{1.x}Sr_xMnO₃ is increased to $102\,\mathrm{F\,g^{-1}}$ as compared with $60\,\mathrm{F\,g^{-1}}$ of pure LaMnO₃ nanoparticles, on adding 15 mol% Sr [47]. A similar characteristic is observed in the EIS spectra of the present study, where the overall resistance of the SrMnO₃ nanofibers are dropped in the presence of dopants, which ultimately resulted in an enhancement in the supercapacitance of the doped nanofibers. The capacitance of SrMnO₃ nanofibers is significantly higher than that of LaMnO₃ nanoparticles, probably because of enhanced surface areas of the electrospun nanofibers.

The construction of asymmetric capacitor for two electrode study is shown in Fig. 10a. The CV analysis of the electrodes were performed separately in 0.5 M $\rm Na_2SO_4$ solution and it is shown in Fig. 10b. The CV (Fig. 10c) analysis of the electrode assembly shows that, the increase in scan rate from 5 to 100 mV s $^{-1}$ subsequently increased the current. As the scan rate is increased, the CV curve is largely deviated from the near

rectangular shape observed at low scan rate. It is due to the insufficient time for the electrolyte species to access the electrode material through the tunnels or pores present [61]. The Galvanostatic charge-discharge curves of the asymmetric supercapacitor is shown in Fig. 10d. The asymmetrical nature of GCD is mainly attributed to the electrochemical oxidation/reduction reaction at the electrode/electrolyte interface, during which Mn⁴⁺ is converted to Mn²⁺ and vice versa [68]. The specific capacitance was calculated using the following equation [69].

$$C = \frac{2I\Delta t}{mV} \tag{4}$$

where I is the discharge current, Δt is discharge time, m is the mass of active material and V is the potential window, respectively. The specific capacity of the supercapacitor device is $420.3\,\mathrm{F\,g^{-1}}$ at a density of $0.5\,\mathrm{A\,g^{-1}}$. Approximately 60% specific capacity is retained when the current density is increased to $2\,\mathrm{A\,g^{-1}}$, as in Fig. 10e. The Nyquist plot of this device is similar to that of the three-electrode system as discussed before.

Specific energy and specific power are calculated for the asymmetric supercapacitor device and the respective Ragone plot is shown in Fig. 10f. Specific energy and specific power determines the power applications of supercapacitor. The Ragone plot for the device is obtained at the potential window of $0.8 \, \text{V}$ in $0.5 \, \text{M}$ $\text{Na}_2 \text{SO}_4$ aqueous solution. The specific energy (E) and specific power (P) are calculated using the following equations [70].

$$E = \frac{CV^2}{2 \times 3.6} \quad (\text{in WhKg}^{-1})$$
 (5)

$$P = \frac{3600 \quad E}{\Delta t} \quad \text{(in WKg}^{-1}\text{)} \tag{6}$$

where C is specific capacitance, V is the potential window and Δt is the discharge time, respectively.

The specific energy decreases with respect to an increase in the specific power as the galvanostatic (GV) charge/discharge current

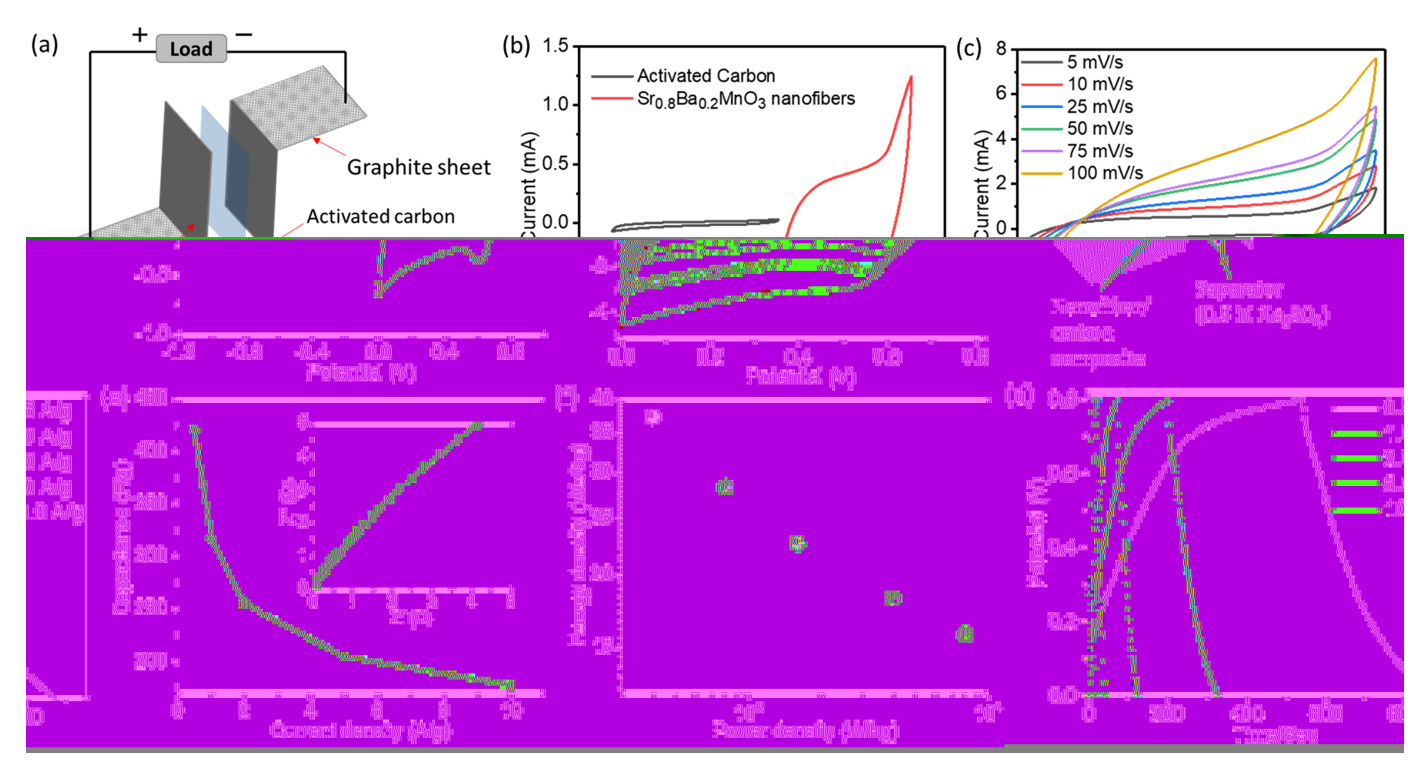


Fig. 10. (a) schematic of the assembly, (b) comparison of CV curves of $Sr_{0.8}Ba_{0.2}MnO_3$ nanofibers as positive electrode and activated carbon as negative electrode, (C) CV curves, (d) Galvanostatic charge/discharge curves at different current densities, (e) specific capacitance at different current densities (Nyquist plot in the inset) and (f) Ragone plot of $Sr_{0.8}Ba_{0.2}MnO_3$ asymmetric supercapacitor.

increased from 0.5 to $10\,\mathrm{A\,g^{-1}}$. The energy density nanofiber supercapacitor is estimated as $37.3\,\mathrm{W\,h\,kg^{-1}}$ at a power density of $400\,\mathrm{W\,kg^{-1}}$. The energy density is $15.7\,\mathrm{W\,h\,kg^{-1}}$ even at a high-power density of $8006\,\mathrm{W\,kg^{-1}}$, indicating the potential of these electrode materials for high-rate charge/discharge operations in supercapacitors. These results are compatible among reported asymmetric devices and similar to perovskite-based supercapacitors [16,21,68,71-73].

Another important requirement for supercapacitor applications is cycling life. The long cycle life is an important parameter for evaluating the performance of a supercapacitor. The long-term cycle ability of the $\rm Sr_{0.8}Ba_{0.2}MnO_3$ nanofiber supercapacitors was evaluated by repeating the charge-discharge test at a current density $10\,\rm A\,g^{-1}$ for 5000 cycles, as shown in Fig. 11, using constant current galvanostatic (GV) charge/discharge cycling techniques in the potential windows ranging from 0 to 0.8 V. The specific capacitance of the $\rm Sr_{0.8}Ba_{0.2}MnO_3$ nanofibers is

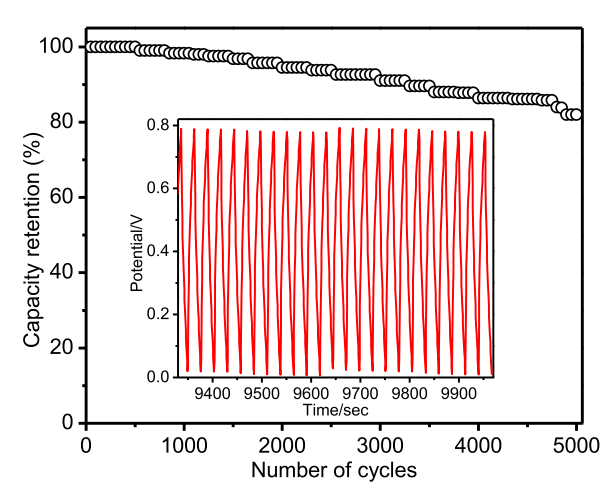


Fig. 11. Cycle stability of the $\rm Sr_{0.8}Ba_{0.2}MnO_3$ supercapacitors at a current density of $\rm 10\,A\,g^{-1}$, inset shows a sample cycling interval.

decayed to 87% after 5000 cycles, illustrating the utilitarian long-term cyclability of the nanofibers as supercapacitor electrode.

4. Conclusions

In conclusion, perovskite SrMnO3 porous nanofibers have been successfully fabricated using a simple sol-gel assisted electrospinning process and calcination. The SrMnO₃ nanofibers calcined at 700 °C exhibit a superior supercapacitance than the nanofibers calcined at other temperatures. The porous nanofibrous morphology is revealed in the SEM analysis, and the nanosized particles composing the nanofibers are observed in TEM analysis. The influence of Ba, Ca, Co, Fe and Ni doping on supercapacitance of SrMnO₃ nanofibers are studied further. The XRD analysis reveals that the obtained SrMnO₃ nanofibers at 700 °C possess a hexagonal structure and the structure is unaltered by the dopant loading until 20 mol%. Doping 20 mol% Ba to SrMnO3 matrix significantly enhance the specific capacitance from 321.7 F $\rm g^{-1}$ to up to 446.8 F g⁻¹ at a discharge current density of 0.5 A g⁻¹. The enhancement in specific capacitance by doping is postulated as the increase in the oxygen vacancies by lattice distortions. An asymmetric capacitor device fabricated using Ba-doped SrMnO₃ nanofibers exhibit a specific capacitance of 423 F g⁻¹ with an energy density of 37.3 Wh kg⁻¹ at a power density 400 W kg⁻¹. The nanofibers retained 87% its initial capacitance after 5000 successive cycles. The superior capacitive properties of 20 mol% Ba doped SrMnO3 nanofibers distinguish them as a promising candidate for supercapacitor applications.

Acknowledgements

The authors would like to thank the U.S. National Science Foundation (NSF) for research funding, award no. HRD 1436120 and 1719511. The instrumentation was supported by the U.S. Department of Defense grants W911NF-14-1-0060, W911NF-15-1-0566 and W911NF-09-1-0011, and the U.S. NSF MRI Program DMR 1626376. Use of the Center for Nanoscale Materials, an Office of Science user facility,

was supported by the U.S. Department of Energy, Office of Science, Office of Basic Energy Sciences, under Contract No. DE-AC02-06CH11357

Appendix A. Supporting information

Supplementary data associated with this article can be found in the online version at doi:10.1016/j.ceramint.2018.08.313.

References

- D. Yu, K. Goh, H. Wang, L. Wei, W. Jiang, Q. Zhang, L. Dai, Y. Chen, Scalable synthesis of hierarchically structured carbon nanotube–graphene fibres for capacitive energy storage, Nat. Nanotechnol. 9 (2014) 555–562, https://doi.org/10. 1038/nnano.2014.93.
- [2] J. Dong, G. Lu, F. Wu, C. Xu, X. Kang, Z. Cheng, Facile synthesis of a nitrogen-doped graphene flower-like MnO₂ nanocomposite and its application in supercapacitors, Appl. Surf. Sci. 427 (2018) 986–993, https://doi.org/10.1016/j.apsusc.2017.07.
- [3] X. Li, G. Wang, X. Wang, X. Li, J. Ji, Flexible supercapacitor based on MnO₂ nanoparticles via electrospinning, J. Mater. Chem. A 1 (2013) 10103–10106 http://dx.doi.org/0.1039/C3TA11227H
- [4] B. Ren, M. Fan, Q. Liu, J. Wang, D. Song, X. Bai, Hollow NiO nanofibers modified by citric acid and the performances as supercapacitor electrode, Electrochim. Acta 92 (2013) 197–204, https://doi.org/10.1016/j.electacta.2013.01.009.
- [5] M. Kumar, A. Subramania, K. Balakrishnan, Preparation of electrospun Co₃O₄ nanofibers as electrode material for high performance asymmetric supercapacitors, Electrochim. Acta 149 (2014) 152–158, https://doi.org/10.1016/j.electacta.2014.10.021
- [6] L.T. Le, M.H. Ervin, H. Qiu, B.E. Fuchs, W.Y. Lee, Graphene supercapacitor electrodes fabricated by inkjet printing and thermal reduction of graphene oxide, Electrochem. Commun. 13 (2011) 355–358, https://doi.org/10.1016/j.elecom. 2011.01.023
- [7] S. Hu, R. Rajamani, X. Yu, Flexible solid-state paper based carbon nanotube supercapacitor, Appl. Phys. Lett. 100 (2012) 104103, https://doi.org/10.1063/1. 3601048
- [8] Z. Lei, N. Christov, X.S. Zhao, Intercalation of mesoporous carbon spheres between reduced graphene oxide sheets for preparing high-rate supercapacitor electrodes, Energy Environ. Sci. 4 (2011) 1866–1873, https://doi.org/10.1039/C1EE01094H.
- [9] K.S. Ryu, K.M. Kim, N.-G. Park, Y.J. Park, S.H. Chang, Symmetric redox supercapacitor with conducting polyaniline electrodes, J. Power Sources 103 (2002) 305–309, https://doi.org/10.1016/S0378-7753(01)00862-X.
- [10] J. Cao, Y. Wang, Y. Zhou, J.-H. Ouyang, D. Jia, L. Guo, High voltage asymmetric supercapacitor based on MnO₂ and graphene electrodes, J. Electroanal. Chem. 689 (2013) 201–206, https://doi.org/10.1016/j.jelechem.2012.10.024.
- [11] Y. Xie, Y. Liu, Y. Zhao, Y.H. Tsang, S.P. Lau, H. Huang, Y. Chai, Stretchable all-solid-state supercapacitor with wavy shaped polyaniline/graphene electrode, J. Mater. Chem. A 2 (2014) 9142–9149, https://doi.org/10.1039/C4TA00734D.
- [12] B. Ding, J. Yu (Eds.), Electrospun Nanofibers for Energy and Environmental Applications, Springer-Verlag, Berlin, 2014, https://doi.org/10.1007/978-3-642-54160-5.
- [13] J. Wang, J. Polleux, J. Lim, B. Dunn, Pseudocapacitive contributions to electrochemical energy storage in TiO₂ (anatase) nanoparticles, J. Phys. Chem. C 111 (2007) 14925–14931, https://doi.org/10.1021/jp074464w.
- [14] A.H. McDaniel, A. Ambrosini, E.N. Coker, J.E. Miller, W.C. Chueh, R. O'Hayre, J. Tong, Nonstoichiometric perovskite oxides for solar thermochemical H₂ and CO production, Energy Procedia 49 (2014) 2009–2018, https://doi.org/10.1016/j. egypro.2014.03.213.
- [15] J. Wang, Y. Gao, D. Chen, J. Liu, Z. Zhang, Z. Shao, F. Ciucci, Water splitting with an enhanced bifunctional double perovskite, ACS Catal. 8 (2018) 364–371, https:// doi.org/10.1021/acscatal.7b02650.
- [16] Y. Liu, J. Dinh, M.O. Tade, Z. Shao, Design of perovskite oxides as anion-intercalation-type electrodes for supercapacitors: cation leaching effect, ACS Appl. Mater. Interfaces 8 (2016) 23774–23783, https://doi.org/10.1021/acsami. 6100624
- [17] P. Tan, M. Liu, Z. Shao, M. Ni, Recent advances in perovskite oxides as electrode materials for nonaqueous lithium–oxygen batteries, Adv. Energy Mater. 7 (2017) 1602674, https://doi.org/10.1002/aenm.201602674.
- [18] Y. Yamada, Y. Kanemitsu, Photoluminescence spectra of perovskite oxide semiconductors, J. Lumin. 133 (2013) 30–34, https://doi.org/10.1016/j.jlumin.2011. 12.037
- [19] C.N.R. Rao, Perovskite oxides and high-temperature superconductivity, Ferroelectrics 102 (1990) 297–308, https://doi.org/10.1080/ 00150199008221489
- [20] N. Arjun, G.-T. Pan, T.C.K. Yang, The exploration of lanthanum based perovskites and their complementary electrolytes for the supercapacitor applications, Results Phys. 7 (2017) 920–926, https://doi.org/10.1016/j.rinp.2017.02.013.
- [21] J.T. Mefford, W.G. Hardin, S. Dai, K.P. Johnston, K.J. Stevenson, Anion charge storage through oxygen intercalation in LaMnO₃ perovskite pseudocapacitor electrodes, Nat. Mater. 13 (2014) 726–732, https://doi.org/10.1038/nmat4000.
- [22] J. Zhu, H. Li, L. Zhong, P. Xiao, X. Xu, X. Yang, Z. Zhao, J. Li, Perovskite oxides: preparation, characterizations, and applications in heterogeneous catalysis, ACS

- Catal. 4 (2014) 2917-2940, https://doi.org/10.1021/cs500606g.
- F. Galasso, Perovskites and High Tc Superconductors, Routledge, New York, 1990.
 Y. Guo, T. Shao, H. You, S. Li, C. Li, L. Zhang, Polyvinylpyrrolidone-assisted solvothermal synthesis of porous LaCoO₃ nanospheres as supercapacitor electrode, Int. J. Electrochem. Sci. 12 (2017) 7121–7127, https://doi.org/10.20964/2017.08.47.
- [25] T. Shao, H. You, Z. Zhai, T. Liu, M. Li, L. Zhang, Hollow spherical LaNiO₃ super-capacitor electrode synthesized by a facile template-free method, Mater. Lett. 201 (2017) 122–124, https://doi.org/10.1016/j.matlet.2017.04.143.
- [26] Collaboration, Authors and editors of the volumes III/17H-17I-41E, LaMnO₃ crystal structure, lattice parameters, physical properties, in: O. Madelung, U. Rössler, M. Schulz (Eds.), Ternary Compounds, Organic Semiconductors, 41E Springer, Berlin, 2000, pp. 1–7, https://doi.org/10.1007/10717201_1101 (pp).
- [27] Y. Cao, B. Lin, Y. Sun, H. Yang, X. Zhang, Sr-doped lanthanum nickelate nanofibers for high energy density supercapacitors, Electrochim. Acta 174 (2015) 41–50, https://doi.org/10.1016/j.electacta.2015.05.131.
- [28] Y. Cao, B. Lin, Y. Sun, H. Yang, X. Zhang, Symmetric/asymmetric supercapacitor based on the perovskite-type lanthanum cobaltate nanofibers with Sr-substitution, Electrochim. Acta 178 (2015) 398–406, https://doi.org/10.1016/j.electacta.2015. 08 033
- [29] X.W. Wang, Q.Q. Zhu, X.E. Wang, H.C. Zhang, J.J. Zhang, L.F. Wang, Structural and electrochemical properties of La_{0.85}Sr_{0.15}MnO₃ powder as an electrode material for supercapacitor, J. Alloy. Compd. 675 (2016) 195–200, https://doi.org/10.1016/j. iallcom.2016.03.048.
- [30] P.M. Wilde, T.J. Guther, R. Oesten, J. Garche, Strontium ruthenate perovskite as the active material for supercapacitors, J. Electroanal. Chem. 461 (1999) 154–160, https://doi.org/10.1016/S0022-0728(98)00179-X.
- [31] K. Karthick, S.R. Ede, U. Nithiyanantham, S. Kundu, Low-temperature synthesis of SrTiO₃ nanoassemblies on DNA scaffolds and their applications in dye-sensitized solar cells and supercapacitors, New J. Chem. 41 (2017) 3473–3486, https://doi. org/10.1039/C7NJ00204A.
- [32] F. Deganello, L.F. Liotta, S.G. Leonardi, G. Neri, Electrochemical properties of Cedoped SrFeO₃ perovskites-modified electrodes towards hydrogen peroxide oxidation, Electrochim. Acta 190 (2016) 939–947, https://doi.org/10.1016/j.electacta. 2015.12.101.
- [33] S. Demirel, E. Oz, S. Altin, A. Bayri, O. Baglayan, E. Altin, S. Avci, Structural, magnetic, electrical and electrochemical properties of SrCoO_{2.5}, Sr₉Co₂Mn₅O₂₁ and SrMnO₃ compounds, Ceram. Int. 43 (2017) 14818–14826, https://doi.org/10.1016/j.ceramint.2017.07.230.
- [34] S. Gholamrezaei, M. Salavati-Niasari, Sonochemical synthesis of SrMnO $_3$ nanoparticles as an efficient and new catalyst for O $_2$ evolution from water splitting reaction, Ultrason. Sonochem. 40 (2018) 651–663, https://doi.org/10.1016/j.ultsonch.2017.08.012.
- [35] A. Aguadero, D. Pérez-Coll, J.A. Alonso, S.J. Skinner, J. Kilner, A new family of Modoped $SrCoO_{3-\delta}$ perovskites for application in reversible solid state electrochemical cells, Chem. Mater. 24 (2012) 2655–2663, https://doi.org/10.1021/cm300255r.
- [36] X. Chen, L. Huang, Y. Wei, H. Wang, Tantalum stabilized $SrCoO_{3-\delta}$ perovskite membrane for oxygen separation, J. Membr. Sci. 368 (2011) 159–164, https://doi.org/10.1016/j.memsci.2010.11.040.
- [37] Y. Wang, J. Chen, X. Wu, Preparation and gas-sensing properties of perovskite-type SrFeO₃ oxide, Mater. Lett. 49 (2001) 361–364, https://doi.org/10.1016/S0167-577X(00)00400-6
- [38] F. Wang, Y.Q. Zhang, Y. Bai, W. Liu, H.R. Zhang, W.Y. Wang, S.K. Li, S. Ma, X.G. Zhao, J.R. Sun, Z.H. Wang, Z.J. Wang, Z.D. Zhang, Oxygen vacancy formation, crystal structures, and magnetic properties of three SrMnO $_{3-\delta}$ films, Appl. Phys. Lett. 109 (2016) 052403, https://doi.org/10.1063/1.4960463.
- [39] K.J. Lee, E. Iguchi, Electronic properties of SrMnO_{3-x}, J. Solid State Chem. 114 (1995) 242–248, https://doi.org/10.1006/jssc.1995.1035.
- [40] J. Heiras, E. Pichardo, A. Mahmood, T. López, R. Pérez-Salas, J.M. Siqueiros, M. Castellanos, Thermochromism in (Ba,Sr)-Mn oxides, J. Phys. Chem. Solids 63 (2002) 591–595, https://doi.org/10.1016/S0022-3697(01)00198-6.
- [41] C. Jeong, J. Ryu, T. Noh, Y.-N. Kim, H. Lee, Structural analysis and electrode performance of Ce doped SrMnO₃ synthesised by EDTA citrate complexing process, Adv. Appl. Ceram. 112 (2013) 494–498, https://doi.org/10.1179/1743676113Y.0000000122
- [42] S. Hashimoto, T. Shimura, H. Iwahara, Electrical properties of Ce-doped SrMnO₃ as a cathode material, Proc. Electrochem. Soc. PV 1999-19 (1999) 379–388, https://doi.org/10.1149/199919.0379PV.
- [43] J. Ryu, R. O'Hayre, H. Lee, Structural analysis and electrochemical properties of cobalt-doped $Sr_{0.9}Ce_{0.1}MnO_{3-\delta}$ cathode for IT-SOFCs, J. Mater. Res. 29 (2014) 2667–2672, https://doi.org/10.1557/jmr.2014.306.
- [44] A. Nemudry, E.L. Goldberg, M. Aguirre, M.Á. Alario-Franco, Electrochemical to-potactic oxidation of nonstoichiometric perovskites at ambient temperature, Solid State Sci. 4 (2002) 677–690, https://doi.org/10.1016/S1293-2558(02)01313-4.
- [45] J. Suntivich, K.J. May, H.A. Gasteiger, J.B. Goodenough, Y. Shao-Horn, A perovskite oxide optimized for oxygen evolution catalysis from molecular orbital principles, Science 334 (2011) 1383–1385, https://doi.org/10.1126/science.1212858.
- [46] J. Suntivich, H.A. Gasteiger, N. Yabuuchi, H. Nakanishi, J.B. Goodenough, Y. Shao-Horn, Design principles for oxygen-reduction activity on perovskite oxide catalysts for fuel cells and metal-air batteries, Nat. Chem. 3 (2011) 546–550, https://doi. org/10.1038/nchem.1069.
- [47] X. Lang, H. Mo, X. Hu, H. Tian, Supercapacitor performance of perovskite La_{1-x}Sr_xMnO₃, Dalton Trans. 46 (2017) 13720–13730, https://doi.org/10.1039/ C7DT03134C.
- [48] Y.K. Du, P. Yang, Z.G. Mou, N.P. Hua, L. Jiang, Thermal decomposition behaviors of PVP coated on platinum nanoparticles, J. Appl. Polym. Sci. 99 (2006) 23–26, https://doi.org/10.1002/app.21886.

- [49] R. Chandrasekar, L. Zhang, J.Y. Howe, N.E. Hedin, Y. Zhang, H. Fong, Fabrication and characterization of electrospun titania nanofibers, J. Mater. Sci. 44 (2009) 1198–1205, https://doi.org/10.1007/s10853-008-3201-1.
- [50] B. Mistry, Handbook of Spectroscopic Data: Chemistry UV,IR,PMR,CNMR and Mass Spectroscopy, Oxford Book Company, New Delhi, 2009.
- [51] Y.-J. Song, M. Wang, X.-Y. Zhang, J.-Y. Wu, T. Zhang, Investigation on the role of the molecular weight of polyvinyl pyrrolidone in the shape control of high-yield silver nanospheres and nanowires, Nanoscale Res. Lett. 9 (2014) 17, https://doi. org/10.1186/1556-2768-9-17.
- [52] N. Pandey, A.K. Thakur, Studies on structural and electrical properties of SrMnO₃₋₈ prepared in oxidising medium, Adv. Appl. Ceram. 109 (2010) 83–90, https://doi.org/10.1179/174367509X12503626841433.
- [53] R.N. Mariammal, K. Ramachandran, G. Kalaiselvan, S. Arumugam, B. Renganathan, D. Sastikumar, Effect of magnetism on the ethanol sensitivity of undoped and Mndoped CuO nanoflakes, Appl. Surf. Sci. 270 (2013) 545–552, https://doi.org/10. 1016/j.apsusc.2013.01.084.
- [54] B. Aurian-Blajeni, A.G. Kimball, L.S. Robblee, G.L.M.K.S. Kahanda, M. Tomkiewicz, Correlation between charge storage capacity and morphology, J. Electrochem. Soc. 134 (1987) 2637–2638, https://doi.org/10.1149/1.2100261.
- [55] G.Z. Chen, Understanding supercapacitors based on nano-hybrid materials with interfacial conjugation, Prog. Nat. Sci.: Mater. Int. 23 (2013) 245–255, https://doi. org/10.1016/j.pnsc.2013.04.001.
- [56] L. Bao, J. Zang, X. Li, Flexible Zn₂SnO₄/MnO₂ core/shell nanocable–carbon microfiber hybrid composites for high-performance supercapacitor electrodes, Nano Lett. 11 (2011) 1215–1220, https://doi.org/10.1021/nl104205s.
- [57] R.B. Rakhi, W. Chen, D. Cha, H.N. Alshareef, Influence of calcination temperature on the morphology and energy storage properties of cobalt oxide nanostructures directly grown over carbon cloth substrates, Mater. Renew. Sustain. Energy 2 (2013) 17, https://doi.org/10.1007/s40243-013-0017-y.
- [58] Z. Wu, L. Li, J. Yan, X. Zhang, Materials design and system construction for conventional and new-concept supercapacitors, Adv. Sci. 4 (2017) 1600382, https://doi.org/10.1002/advs.201600382.
- [59] S. Kato, M. Ogasawara, M. Sugai, S. Nakata, Crystal structure and property of perovskite-type oxides containing ion vacancy, Catal. Surv. Asia 8 (2004) 27–34, https://doi.org/10.1023/B:CATS.0000015112.82947.8e.
- [60] B. Halperin, R. Englman, Cooperative dynamic Jahn-Teller effect. II. Crystal distortion in perovskites, Phys. Rev. B 3 (1971) 1698–1708, https://doi.org/10.1103/PhysRevB.3.1698.
- [61] P.M. Shafi, N. Joseph, A. Thirumurugan, A.C. Bose, Enhanced electrochemical performances of agglomeration-free LaMnO₃ perovskite nanoparticles and achieving high energy and power densities with symmetric supercapacitor design, Chem. Eng. J. 338 (2018) 147–156, https://doi.org/10.1016/j.cej.2018.01.022.
- [62] A. Laheäär, P. Przygocki, Q. Abbas, F. Béguin, Appropriate methods for evaluating

- the efficiency and capacitive behavior of different types of supercapacitors, Electrochem. Commun. 60 (2015) 21–25, https://doi.org/10.1016/j.elecom.2015. 07.022.
- [63] J. Chang, W. Lee, R.S. Mane, B.W. Cho, S.-H. Han, Morphology-dependent electrochemical supercapacitor properties of indium oxide, Electrochem. Solid-State Lett. 11 (2008) A9–A11, https://doi.org/10.1149/1.2805996.
- [64] C. Guan, J. Liu, C. Cheng, H. Li, X. Li, W. Zhou, H. Zhang, H.J. Fan, Hybrid structure of cobalt monoxide nanowire @ nickel hydroxidenitrate nanoflake aligned on nickel foam for high-rate supercapacitor, Energy Environ. Sci. 4 (2011) 4496–4499, https://doi.org/10.1039/C1EE01685G.
- [65] S. Hébert, B. Wang, A. Maignan, C. Martin, R. Retoux, B. Raveau, Vacancies at Mnsite in Mn³⁺ rich manganites: a route to ferromagnetism but not to metallicity, Solid State Commun. 123 (2002) 311–315, https://doi.org/10.1016/S0038-1008(22)00243-0
- [66] Z.A. Elsiddig, H. Xu, D. Wang, W. Zhang, X. Guo, Y. Zhang, Z. Sun, J. Chen, Modulating Mn⁴⁺ ions and oxygen vacancies in nonstoichiometric LaMnO₃ perovskite by a facile sol-gel method as high-performance supercapacitor electrodes, Electrochim. Acta 253 (2017) 422–429, https://doi.org/10.1016/j.electacta.2017. 09 076
- [67] N. Maheswari, G. Muralidharan, Supercapacitor behavior of cerium oxide nanoparticles in neutral aqueous electrolytes, Energy Fuels 29 (2015) 8246–8253, https://doi.org/10.1021/acs.energyfuels.5b02144.
- [68] S. Nagamuthu, S. Vijayakumar, K.-S. Ryu, Cerium oxide mixed LaMnO₃ nano-particles as the negative electrode for aqueous asymmetric supercapacitor devices, Mater. Chem. Phys. 199 (2017) 543–551, https://doi.org/10.1016/j.matchemphys. 2017.07.050.
- [69] E. Frackowiak, V. Khomenko, K. Jurewicz, K. Lota, F. Béguin, Supercapacitors based on conducting polymers/nanotubes composites, J. Power Sources 153 (2006) 413–418, https://doi.org/10.1016/j.jpowsour.2005.05.030.
- [70] M. Rajkumar, C.-T. Hsu, T.-H. Wu, M.-G. Chen, C.-C. Hu, Advanced materials for aqueous supercapacitors in the asymmetric design, Prog. Nat. Sci.: Mater. Int. 25 (2015) 527–544, https://doi.org/10.1016/j.pnsc.2015.11.012.
- [71] G.W. Piburn, J.T. Mefford, N. Zinni, K.J. Stevenson, S.M. Humphrey, Synthesis and charge storage properties of templated LaMnO₃–SiO₂ composite materials, Dalton Trans. 46 (2017) 977–984, https://doi.org/10.1039/C6DT04665G.
- [72] P.M. Shafi, V. Ganesh, A.C. Bose, LaMnO₃/RGO/PANI ternary nanocomposites for supercapacitor electrode application and their outstanding performance in all-solidstate asymmetrical device design, ACS Appl. Energy Mater. 1 (2018) 2802–2812, https://doi.org/10.1021/acsaem.8b00459.
- [73] J. Hu, L. Shi, Q. Liu, H. Huang, T. Jiao, Improved oxygen reduction activity on silver-modified LaMnO₃-graphene via shortens the conduction path of adsorbed oxygen, RSC Adv. 5 (2015) 92096–92106, https://doi.org/10.1039/C5RA14928B.